A Monolithic Compliant Continuum Manipulator

Thomas, Theodosia Lourdes; Venkiteswaran, Venkatasubramanian Kalpathy; Ananthasuresh, G. K.; Misra, Sarthak

Published in:
Journal of mechanisms and robotics-Transactions of the asme

DOI:
10.1115/1.4046838

Theodosia Lourdes Thomas[1]
Surgical Robotics Laboratory,
Department of Biomechanical Engineering,
University of Twente,
7500 AE Enschede, The Netherlands
e-mail: t.l.thomas@utwente.nl

Venkatasubramanian Kalpathy Venkiteswaran
Surgical Robotics Laboratory,
Department of Biomechanical Engineering,
University of Twente,
7500 AE Enschede, The Netherlands
e-mail: v.kalpathyvenkiteswaran@utwente.nl

G. K. Ananthasuresh
Multidisciplinary and Multiscale Device and Design Lab,
Department of Mechanical Engineering,
Indian Institute of Science,
Bengaluru 560012, Karantaka, India
e-mail: suresh@iisc.ac.in

Sarthak Misra
Surgical Robotics Laboratory,
Department of Biomechanical Engineering,
University of Twente,
7500 AE Enschede, The Netherlands;
Department of Biomedical Engineering,
University of Groningen,
University Medical Centre Groningen,
9713 GZ Groningen, The Netherlands
e-mail: s.misra@utwente.nl

A Monolithic Compliant Continuum Manipulator: A Proof-of-Concept Study

Continuum robots have the potential to form an effective interface between the patient and surgeon in minimally invasive procedures. Magnetic actuation has the potential for accurate catheter steering, reducing tissue trauma and decreasing radiation exposure. In this paper, a new design of a monolithic metallic compliant continuum manipulator is presented, with flexures for precise motion. Contactless actuation is achieved using time-varying magnetic fields generated by an array of electromagnetic coils. The motion of the manipulator under magnetic actuation for planar deflection is studied. The mean errors of the theoretical model compared to experiments over three designs are found to be 1.9 mm and 5.1 deg in estimating the in-plane position and orientation of the tip of the manipulator, respectively, and 1.2 mm for the whole shape of the manipulator. Maneuverability of the manipulator is demonstrated by steering it along a path of known curvature and also through a gelatin phantom, which is visualized in real time using ultrasound imaging, substantiating its application as a steerable surgical manipulator.
[DOI: 10.1115/1.4046838]

Keywords: compliant mechanisms, mechanism design, medical robotics, robot design

1 Introduction

The field of continuum robots has seen significant growth in the last few decades. The designs of snakes, elephant trunks, and octopus tentacles have encouraged researchers to devise bio-inspired hyperreduntant robots for dexterous manipulation of objects [1]. Continuum robots have great potential within medical applications and for robot-assisted minimally invasive surgery (MIS), in particular. In the current literature, the focus is on designing miniaturized manipulators, which are sufficiently flexible to be steered inside the body and reach difficult-to-access surgical sites with high dexterity. Such devices find applications in neurosurgery, endoscopy, laparoscopy, biopsy, and other surgical procedures in which these devices enter the body through small incisions [2,3].

There is a growing body of literature that demonstrates many applications of continuum manipulators in MIS with different designs [4]. For example, concentric-tube robots having multiple tubes of different predetermined curvature and stiffness cover wide geometry that enables surgical dexterity [5]. Burgner et al. [6] showed that an interchangeable inner tube enables easy sterilization. However, tackling snapping behavior of concentric-tube robots during manipulation remains a challenge [7]. A teleoperated multibackbone continuum manipulator with multiple instrumentation channels has been demonstrated by Goldman et al. [8], and Yang and coworkers [9] developed a snake-inspired robot for performing complex endoscopic tasks. Nonetheless, piston-lead screw actuation units have inherent backlash, which reduces positioning accuracy, and tendon-driven systems are difficult to miniaturize. Other commercially available systems such as the Sensei X by Hansen Medical, Inc. (CA) have demonstrated significant advantage in the reduction of X-ray exposure [10,11]. As the radiation exposure time of patients and physicians depends on the complexity of the procedure, such remote navigation systems have the potential to assist surgeons perform their task quickly without direct intervention [12,13].

Over the years, surgical instruments based on the compliant mechanisms have gained significant attention [14]. The use of monolithic mechanism designs reduces the number of assembly steps, thereby simplifying the fabrication process and reducing maintenance [15]. Relative motion between members is eliminated, leading to high precision, reduction in wear, friction, backlash, noise, while rendering lubrication nonessential [16]. A number of compliant mechanisms utilize flexure hinges, which are flexible members that enable limited relative rotation between two adjacent rigid members [17]. Yin and Anathasuresh have previously demonstrated the virtues of distributed compliance in flexure-based mechanisms, reducing peak stresses in the system and achieving restrained uniform local deformation [18]. Thus, flexure-based designs with reduced stress and limited local deformation have potential for application in design of surgical devices. For instance, Swaney et al. [19] have designed a flexure-based steerable needle that minimizes tissue damage, and Chandrasekaran et al. [20] and Chandrasekaran and Thondiyath [21] have developed flexure-based designs of surgical tooltip combined with magnetic coupling and tether-driven power transmission. Previously, Kim et al. have designed a continuum manipulator using creative slotting patterns

[1]Corresponding author.

Contributed by the Mechanisms and Robotics Committee of ASME for publication in the Journal of Mechanisms and Robotics. Manuscript received September 12, 2019; final manuscript received March 21, 2020; published online May 12, 2020. Assoc. Editor: Guimin Chen.

of narrow necked flexures resulting in discrete compliance [22]. Flexure-based designs are also found in the backbone structures of endoscopic continuum robot designed by Kato et al. [23] and the Artisan Extend Control Catheter by Hansen Medical, Inc. (CA) [10], which are tendon-driven devices.

Recently, several studies have proposed magnetic actuation of surgical devices due to the advantages offered by contactless actuation, leading to compact designs [24,25]. Static or low-frequency magnetic fields are also suitable for surgical environments because they are not harmful to humans. Commercial systems using remote magnetic navigation (RMN) are available, such as the Niobe magnetic navigation system (Stereotaxis, Inc., St. Louis, MO) for ablation procedures with catheters equipped with small permanent magnets [26–28]. Multiple studies have been conducted on the use of RMN and magnetic control strategies for surgical manipulators [29–32]. This has heightened the need for versatile designs of magnetic catheters, which are dexterous and multifunctional to perform complex surgical procedures [33–35].

This paper describes a new design of a metallic compliant continuum manipulator capable of planar and spatial bending. The design entails a novel slotting pattern to make a segmented continuum manipulator that is capable of bending about two axes and is cut out of a monolithic tube without using assembly. The objective of this research is to demonstrate the use of a monolithic flexure-based continuum manipulator capable of precise motion using contactless actuation, thereby eliminating undesired backlash and friction, with the potential for further miniaturization. The monolithic compliant design of manipulator enables easy modeling due to linear load-deformation characteristics at individual segments of the manipulator. In contrast to other designs in the literature, the manipulator described here has built-in mechanical motion constraints that restrict the maximum stress in the flexure, thereby maintaining the strength of the manipulator and leading to distributed compliance. In this work, three designs of the planar bending manipulator design are fabricated. Each of them is actuated using controlled magnetic fields by attaching a permanent magnet at its tip. Experiments are conducted to examine the motion characteristics of the manipulator under the influence of actuation loads. The potential of the manipulator as a flexible surgical manipulator, which can be steered inside the body is also demonstrated. A conceptual schematic of the continuum manipulator in a surgical application actuated by electromagnetic coils is shown in Fig. 1.

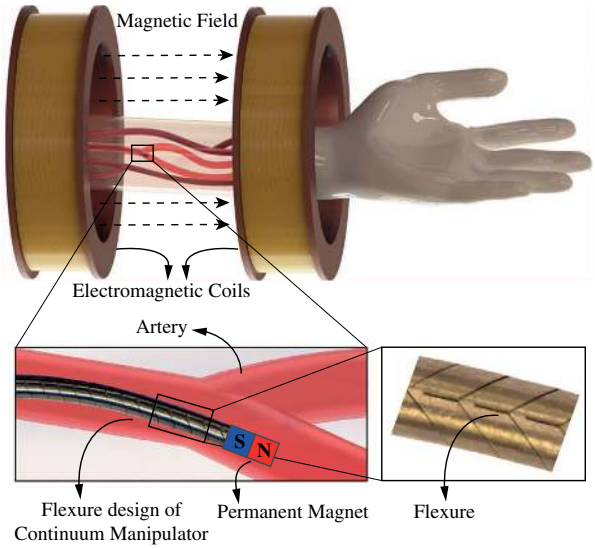

Fig. 1 An illustration of the continuum manipulator being guided inside the arterial system of forearm by a pair of electromagnetic coils. The inset shows the continuum manipulator with a magnet at its end. The inset of the manipulator shows the flexures.

2 Design of the Continuum Manipulator

In this section, the design of the metallic continuum manipulator is described. The concept of the flexures with limited range of motion is presented, followed by the details for single-axis bending, two-axis bending, and the fabrication method.

The body of the manipulator is made from a hollow metallic tube with a series of flexures created by cuts along its length, with each flexure forming an elastic rotational pair. Figure 2(*a*) shows a schematic of the design, with the inset showing a cut section. The range of motion of each flexure is physically constrained by the nature of the cut, thereby limiting the maximum stress in the flexure and preventing failure. The flexures enable bending of the manipulator about the axis perpendicular to the plane of section.

2.1 Single-Axis Bending Design. For achieving rotation about one axis, all flexures are aligned to bend in the same plane. Consider the design shown in Fig. 2(*a*): it consists of N flexures along the manipulator of length (L). The hollow tube has inner radius (r) and outer radius (R). Each flexure is a thin plate having length (l), width (w), and thickness ($t = R - r$). The thin plate can be approximately modeled as a cantilever beam. Each beam (i) is restricted to bend such that its tip displacement (δ_i) is limited to the width of the cut (w_c). The cut into the tube is made at an angle (ψ) to the length of the flexure. Since the flexures are designed such that $w_c << l$, linear load–displacement relationships are applicable. For the purpose of design, the flexures are assumed to undergo pure bending (no shear loads) due to the actuation method used in this paper. Thus, the maximum tip displacement of the flexure (i) is as follows:

$$\delta_i^{max} = \frac{M_i l^2}{2EI} = w_c \tag{1}$$

where M_i is the internal bending moment in flexure i and E is the elastic modulus of the material. The second moment of area of the flexure's cross section (I) is given by $I = w^3 t/12$.

Each flexure (i) rotates by an angle (θ_i) with respect to the preceding beam ($i-1$). The maximum deflection angle of each flexure (θ_i^{max}) is given by,

$$\theta_i^{max} = \frac{M_i l}{EI} \tag{2}$$

Substituting Eq. (1) into Eq. (2) yields,

$$\theta_i^{max} = \frac{2w_c}{l} \tag{3}$$

Since each segment of length (L_i) rotates by a maximum angle (θ_i^{max}), the manipulator of length (L) can undergo a total maximum rotation (θ^{max}), which is expressed as follows:

$$\theta^{max} = \frac{L}{L_i}\theta_i^{max} \tag{4}$$

Additionally, to ensure that the manipulator does not fail, the stress in each flexure must be limited to well below the yield stress (σ_y) of the material. The maximum stress in the manipulator (σ_{max}) and factor of safety (FoS) are calculated as follows:

$$\sigma_{max} = \frac{M_i w}{2I} = E\frac{w_c w}{l^2} \tag{5}$$

$$FoS = \frac{\sigma_y}{\sigma_{max}} \tag{6}$$

For planar bending, we assume $L_i = 1.5l$ between two consecutive beams for sufficient spacing, and the angle (ψ) is set to 135 deg.

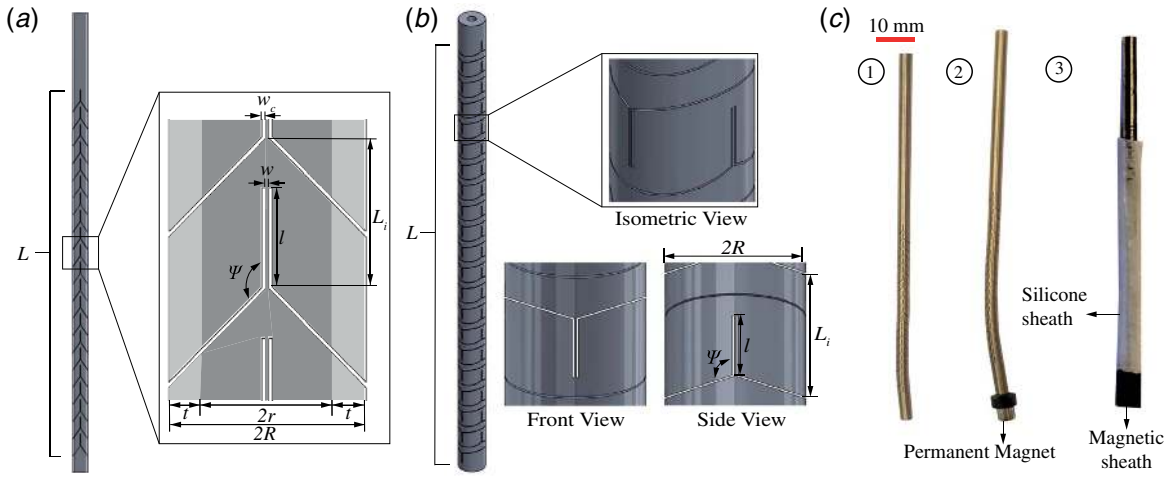

Fig. 2 (*a*) Front view and section view of cross section of single-axis bending design of manipulator. (*b*) The isometric, front and side views of two-axis bending design of manipulator. (*c*) ① Fabricated design A of manipulator, ② design A with permanent magnet at the tip, and ② design A with silicone sheath and magnetic sheath.

Therefore,

$$\theta^{max} = \frac{L}{1.5l}\left(\frac{2w_c}{l}\right) = \frac{4}{3}\frac{Lw_c}{l^2} \tag{7}$$

Therefore, for a required maximum deflection (θ^{max}), the length of each flexure is given by

$$l = \sqrt{\frac{4}{3}\frac{Lw_c}{\theta^{max}}} \tag{8}$$

This implies that the size of the flexure depends on the total length of the manipulator and the desired deflection of manipulator. These parameters can be fine-tuned to achieve a suitable design. Additionally, the critical load for buckling (P_{cr}) is calculated using Euler's formula as follows:

$$P_{cr} = \frac{\pi^2 EI}{l^2} \tag{9}$$

2.2 Two-Axis Bending Design. In order to achieve spatial bending, the flexures must be cut into two planes orthogonal to each other so as to permit rotation about two axes perpendicular to the longitudinal axis of the tube. The isometric, front, and side views of such a design are shown in Fig. 2(*b*). The directions of the cuts into the tube for each axis are reversed to make the design more compact, and the angle of cut (ψ) is reduced to 110 deg. In order to accommodate the orthogonal cuts, the length of each segment is set to $L_i = l - 3R\cos(\psi)$.

The equations for each flexure (1)–(6) also hold for the spatial design. It is inferred from Eq. (3) that with increase in the width of cut (w_c), the maximum angular deflection (θ^{max}) increases. However, the factor of safety (*FoS*) decreases with increasing w_c, as observed in Eqs. (5) and (6). This is evident in the contour plots showing the effect of different design parameters on factor of safety in Fig. 3. In Fig. 3(*a*), sharp changes in *FoS* are observed over a range of w and w_c. This is because the number of flexures (N) can only take whole integer values. The final design parameters are determined through a trade-off between *FoS* and θ^{max}. Titanium grade 2 ($E = 105$ GPa, $\sigma_y = 345$ MPa) is chosen as the material. The resultant parameters are listed in Table 1. It has $N = 20$ flexures for bending along each orthogonal plane and is designed for a deflection of $\theta^{max} = 60$ deg.

To validate the concept, one segment of the two-axis design is analyzed using finite element software (Workbench 16.2, Ansys Inc., Canonsburg, PA). The model is meshed using SOLID187 3-D 10-node elements with a minimum edge length of 0.01 mm. The bottom end is constrained, and a rotational displacement is applied at the top. The combined bending case is tested by a tip rotation of 3 deg (θ^{max}/N) to both flexures. The results are shown in Fig. 4. The maximum stress when both flexures are at maximum deflection is 101.16 MPa, while the stress calculated using Eq. (5) is 99.82 MPa with FoS = 3.51. Therefore, the proposed design is considered safe, and the theoretical stress prediction using the beam model is tenable.

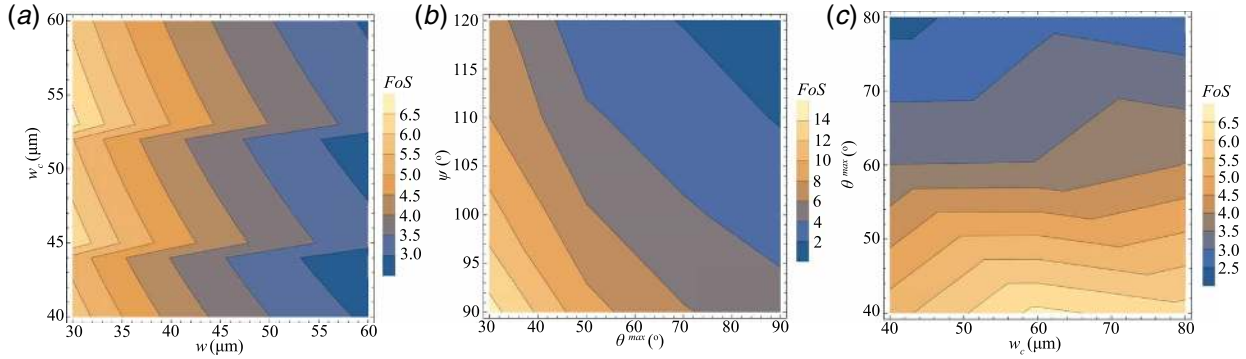

Fig. 3 Contour plots showing the effect on FoS over a varying range of (*a*) width of flexure (w) and width of cut (w_c), for maximum angular deflection (θ^{max}) = 60 deg and angle of cut (ψ) = 110 deg; (*b*) θ^{max} and ψ, for $w = 50\ \mu$m and $w_c = 40\ \mu$m; and (*c*) w_c and θ^{max}, for $w = 50\ \mu$m and $\psi = 110$ deg

Table 1 Design parameters for two-axis bending design as shown in Fig. 2

l (mm)	L (mm)	w (μm)	w_c (μm)	N	FoS	P_{cr} (N)
1.46	60	50	40	20	3.51	10.11

Note: N, FoS, and P_{cr} are the number of flexures, factor of safety, and critical load for buckling, respectively.

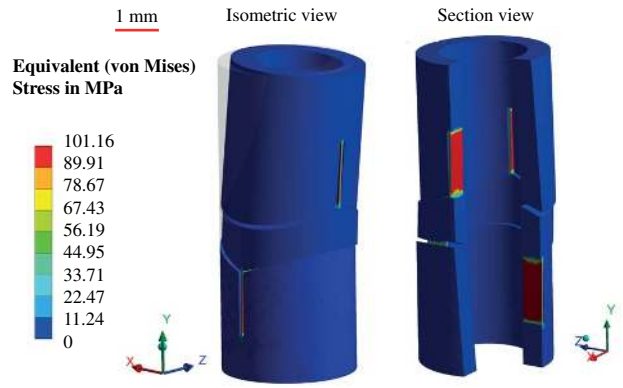

Fig. 4 Stress analysis of a single segment of the two-axis bending design using finite element software. Isometric view shows spatial deflection of the tube under combined loading, while the section view demonstrates that the bending stresses are limited to the flexures.

2.3 Fabrication. For demonstrating the concept, the design of single-axis bending manipulator is adopted as it involves a relatively less complex fabrication process, compared to the two-axis design. Titanium (grade 2) is chosen for fabrication, due to its high ratio of yield strength to elastic modulus ($\sigma_y = 345$ MPa and $E = 105$ GPa) and low weight ratio [36]. Furthermore, it can be used in medical applications due to its nontoxic nature. A hollow titanium tube of outer diameter 3 mm and wall thickness 0.5 mm is used here. The flexures are cut along the tube using the technique of wire electrical discharge machining (EDM). The diameter of the wire used in EDM determines the width of cut (w_c). Three single-axis (planar) bending designs are demonstrated in this paper: their dimensions and properties as listed in Table 2. The flexures are made along a length of 47.5 mm for design A, leaving 7.5 mm without flexures at the end. For design B and design C, flexures are made along a length of 45 mm and 42 mm, respectively. The three fabricated designs have FoS > 3 as determined using Eq. (6).

In addition, a protective sheath is designed for the manipulator to prevent environmental debris from limiting its function during operation. An outer lumen of thickness 0.5 mm is made from silicone rubber (Ecoflex™ 00-10, Smooth-On, Inc., Macungie, PA), having a low elastic modulus ($E_s = 55$ kPa). The silicone rubber sheath is cured in molds made from 3D printed acrylonitrile butadiene styrene parts. The fabricated manipulator with the sheath is shown in Fig. 2(*c*).

Table 2 Fabricated design parameters for single-axis bending design as shown in Fig. 2

Manipulator	l (mm)	w (μm)	w_c (μm)	N	θ_{max} (deg)	FoS	P_{cr} (N)
Design A	1.5	40	55	21	53.58	3.03	2.45
Design B	1.5	65	40	20	36.09	3.12	10.54
Design C	1.1	30	40	23	39.83	3.36	1.92

3 Magnetic Actuation and Test Setup

In this section, a theoretical model is derived to calculate the deflection of the manipulator under the influence of an actuating magnetic field. This is followed by the description of the test setup.

3.1 Magnetic Actuation of the Manipulator. A controlled magnetic field is used to actuate the manipulator. To predict the deflection of the manipulator, a theoretical model based on the principle of minimum potential energy is used. Consider a manipulator fixed at one end and suspended vertically with a permanent magnet of magnetic dipole moment (μ) at its tip (Fig. 5(*a*)). When a magnetic field (B) is applied at an angle (ϕ) to the vertical plane ($x-z$ plane), the permanent magnet experiences a torque (τ) that tries to align it to the direction of external field. This causes the flexures to bend resulting in the deflection of manipulator.

The deflection of the manipulator is calculated using a pseudo-rigid body model. Each segment is approximated by a rigid link of length (L_i), with an associated bending stiffness (K_i). When the manipulator is covered by the polymer sheath, the overall stiffness of each segment is the sum of stiffnesses of the flexure (K_i^f) and the sheath (K_i^s).

$$K_i = 2K_i^f + K_i^s \tag{10}$$

$$K_i^f = \frac{EI}{l}, \quad K_i^s = \frac{E_s I_s}{L_i} \tag{11}$$

Here, E, I, and l are the elastic modulus of Titanium (grade 2), second moment of area of the flexure's cross section, and length of flexure, respectively. E_s and I_s are the approximate linear elastic modulus of the polymer sheath and the second moment of area of its cross section, respectively. Note that there are two flexures in each segment, one on either side of the manipulator.

The principle of minimum potential energy is used to analyze the deflection of the manipulator. The manipulator has N segments, each with a mass (m_i) that deflects by an angle (θ_i). Since the manipulator is held vertically, we consider the effect of gravity in this model. The total potential energy of the system is given by $\Pi = U - W_{ext}$. Here, U is the elastic energy of the system that is the strain energy in the flexures. W_{ext} is the work done by the external forces, which is equal to the sum of work done by gravity (W_g) and

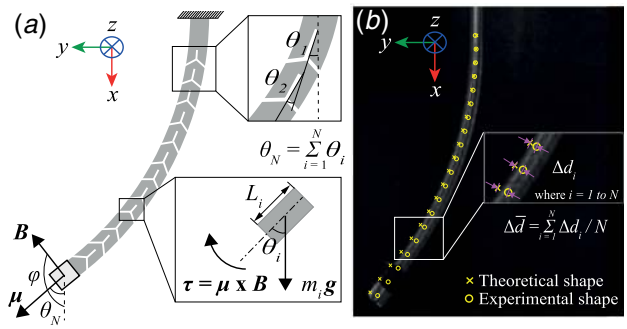

Fig. 5 The manipulator is fixed at top, and a permanent magnet having dipole moment (μ) is attached to its tip. (*a*) Free body diagram: under the influence of magnetic field B acting at an angle (ϕ), the manipulator deflects by an angle (θ_N). Top inset shows the deflection (θ_i) of each flexure. Bottom inset shows a rigid link with gravitation force ($m_i\ g$) acting at its center of mass and torque due to the magnetic field (τ). (*b*) Camera image of design C taken during static experiments: the 'x' and 'o' markers indicate the theoretical and experimental shape estimate of the manipulator, respectively. The inset shows the calculation of whole shape estimation errors (Δd_i) for i points on the manipulator. Mean whole shape estimation error ($\Delta\bar{d}$) is calculated as the average of Δd_i for N points on the manipulator.

the work done by magnetic field (W_μ). This results in

$$\Pi = U - W_g - W_\mu \tag{12}$$

where

$$U = \sum_{i=1}^{N} \frac{1}{2} K_i \theta_i^2 \tag{13}$$

$$W_g = \sum_{i=1}^{N} m_i g x_i + m_\mu g x_\mu \tag{14}$$

$$W_\mu = \int_0^{\theta_N} \tau d\theta = \int_0^{\theta_N} \mu B \sin(\phi - \theta) d\theta$$
$$= \mu B \left[\cos\left(\sum_{i=1}^{N} \theta_i - \phi \right) - \cos(\phi) \right] \tag{15}$$

where location of center of mass of each segment (x_i, y_i) is computed using forward kinematics as follows:

$$x_i = x_{i-1} + L_i \left[\cos(\theta_1) + \cos(\theta_1 + \theta_2) + \cdots + \cos\left(\sum_{1}^{i} \theta_i \right) \right]$$
$$y_i = y_{i-1} + L_i \left[\sin(\theta_1) + \sin(\theta_1 + \theta_2) + \cdots + \sin\left(\sum_{1}^{i} \theta_i \right) \right] \tag{16}$$

Similarly the weight of the last segment and the magnet (m_μ) act at its center of mass distance (L_{CoM}), whose x-coordinate is given by

$$x_\mu = x_N + L_{CoM} \cos\left(\sum_{i=1}^{N} \theta_i \right) \tag{17}$$

Variation of Eqs. (15)–(17) with respect to θ_j (where $j = 1, 2, \ldots, N$) results in

$$\frac{\partial W_\mu}{\partial \theta_j} = \mu B \left[\sin\left(\phi - \sum_{i=1}^{N} \theta_i \right) \right] \tag{18}$$

$$\frac{\partial x_i}{\partial \theta_j} = \begin{cases} 0 & \text{if } i < j \\ -L_i \sum_{k=i}^{j} \sin\left(\sum_{1}^{k} \theta_k \right) & \text{if } j \le i \le N \end{cases} \tag{19}$$

$$\frac{\partial x_\mu}{\partial \theta_j} = -L_i \sum_{k=i}^{N} \sin\left(\sum_{1}^{k} \theta_k \right) - L_{CoM} \sin\left(\sum_{k=1}^{N} \theta_k \right) \tag{20}$$

The principle of minimum potential energy states that the variation of total potential energy is zero, that is, $\partial\Pi = 0$. Substituting Eqs. (18)–(20) in variation of Eq. (12) with respect to θ_j gives N equations as follows:

$$K_i \theta_i = m_i g \sum_{i=1}^{N} \frac{\partial x_i}{\partial \theta_j} + m_\mu g \frac{\partial x_\mu}{\partial \theta_j} + \mu B \sin\left(\phi - \sum_{i=1}^{N} \theta_i \right) \tag{21}$$

This forms a system of equations in θ_j (where $j = 1, 2, \ldots, N$) with the constraint: $-\theta^{max}/N \le \theta_j \le \theta^{max}/N$, where θ_{max} is the total rotation angle observed at maximum deflection of the manipulator (mechanical rotational limit of each segment). If the actuation magnetic field is known (B and ϕ), we can solve the preceding system of equations to obtain the position and the orientation of the manipulator by this model.

3.2 Test Setup. For magnetic actuation, two methods of incorporating magnetic properties on the manipulator are tested. In the first method, a permanent magnet (radius = 2 mm, height = 5 mm, and $\mu = 0.06$ Am^2) is fit at the tip of the manipulator. In the other method, a magnetic sheath of thickness 0.5 mm and length 5 mm is made to cover the manipulator's tip. It is made by fusing ferromagnetic particles (praseodymium–iron–boron: PrFeB, with a mean particle size of 5 μm, Magnequench GmbH, Germany) into the silicone rubber in 1:1 ratio. The cured polymer is subjected to an external magnetic field of 1 T (B-E 25 electromagnet, Bruker Corp., Billerica, MA) to align the magnetic dipoles, forming a soft polymer magnet [37]. These two designs are shown in Fig. 2(*c*).

The setup used here consists of two pairs of Helmholtz coils to generate uniform magnetic fields. Each pair consists of two identical electromagnetic coils as shown in Fig. 6. The first pair of coils generates a uniform magnetic field along the y-axis. The second pair of smaller coils is placed inside the first pair to produce a field along the x-axis. Two cameras are placed in the setup to monitor the front and side view of the workspace.

4 Experiments and Results

The deformation characteristics of the three designs of manipulator under magnetic actuation are evaluated using experiments. The theoretical and experimental results are compared to substantiate the open-loop actuation of manipulator under the influence of magnetic field. Section 4.1 presents the static experiments carried out to analyze the motion of manipulator. Sections 4.2 and 4.3 are part of a feasibility study of the manipulator, which demonstrates the steering of manipulator along a path of known curvature and through gelatin phantom with ultrasound visualization, respectively.

4.1 Static Experiments. The manipulator with a permanent magnet at its tip is suspended vertically at the center of magnetic setup. It is subjected to a magnetic field (B) of constant magnitude. The angle of the magnetic field to the vertical plane (ϕ) is varied to

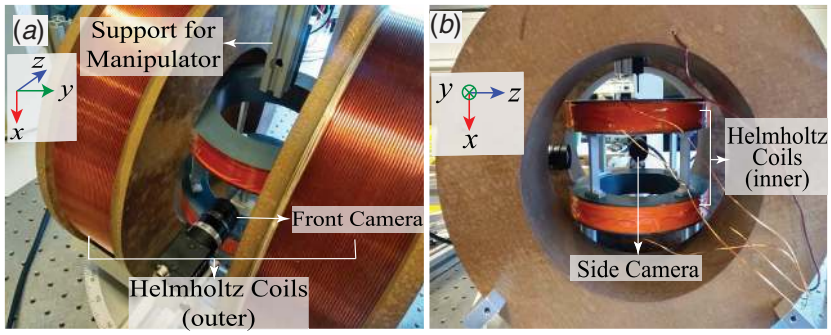

Fig. 6 Experimental setup of two-axis Helmholtz coil setup used for generating magnetic fields: (*a*) front view and (*b*) side view

control the tip angle of the manipulator. The theoretical deformation of the manipulator is calculated using Eq. (21), with x and y coordinates determined using Eq. (16). The experiments were carried out without the polymer sheath, hence, from Eq. (10), we use $K_i = 2K_i^f$. The experimental deflected shape of manipulator is obtained using camera images acquired at various instants of its motion. An image-processing algorithm tracks several points along the length of the manipulator based on a threshold set on pixel intensity. A cubic polynomial curve is fit using these points, which forms the shape of a manipulator. The experimental values of position (x, y) of the manipulator are obtained from the cubic curve equation, and its slope gives the orientation (θ). Figure 5(*b*) is a camera image acquired during the experiment showing the theoretical and experimental shape estimate of the manipulator.

The plots of x and y coordinates, deflection θ of the tip of manipulator, and mean whole shape estimation error ($\Delta\bar{d}$) for the three designs are shown in Fig. 7. The mean and standard deviation of errors between the two sets of data are presented in Table 3. Designs A, B, and C permit a maximum deflection of 54 deg, 36 deg, and 40 deg, respectively.

4.2 Manipulator Steering. In this section, the steerability of the manipulator under open-loop actuation is demonstrated. The length of the manipulator within the workspace is controlled using a linear slide (LX20, Misumi Group Inc., Tokyo, Japan), which is fixed vertically at the top support. The linear slide is powered by a brushless DC motor (maxon EC-max, Maxon Motor, Switzerland) connected to a 24 V power supply. The manipulator with a permanent magnet at its tip is deflected by the magnetic field to control its direction. To follow the path of particular curvature, the manipulator is turned by an angle (θ_N) by applying an actuation field of $B = 20$ mT at an angle (ϕ), calculated using Eq. (21). The manipulator is steered with a polymer sheath covering its body to show clinical feasibility, hence, from Eq. (10), we use $K_i = K_i^s + 2K_i^f$. Figure 8 illustrates the snippets of the video recorded of controlled steering motion of the manipulator.

4.3 Ultrasound Visualization. In this section, steering of the manipulator using real-time ultrasound visualization is demonstrated. A channel of width 10 mm and curvature 45 deg is created inside a phantom made by mixing 8% (by weight) gelatin powder (Technical grade, Boom B.V., The Netherlands) with distilled water. The channel is filled with water, and the manipulator with the permanent magnet at its tip is inserted through it using the linear slide. The direction of manipulator is controlled by changing the orientation of magnetic field, which is provided by user input. The phantom is imaged using a 14 MHz multi-D matrix probe (14L5 transducer) connected to a 2D medical ultrasound machine (SIEMENS AG, Erlangen, Germany). Figure 9 shows the snapshots from the ultrasound imaging of manipulator insertion.

4.4 Discussion. From the results of static experiments (Table 3), it is seen that design B has the highest error. This may be due to its greater width of beam (w) than the width of cut, which restricts the motion of the flexure. Design A has a greater width of cut (w_c) compared to the other two designs, which allows it to achieve larger deflections. Design C has smaller width of beam, which makes it more susceptible to deformation. These factors have to be taken into account for developing an optimized design.

It is also observed that there is a difference in bending curvature between the two half cycles of motion of manipulator, that is, the deflection in the $+y$ direction is different from that in the $-y$ direction. This may be attributed to the manipulator not being exactly straight in the neutral position due to errors in fabrication. When observed under a microscope, it is noticeable that some of the flexures have buckled slightly, suggesting potential plastic deformation (Fig. 10). This can be avoided by using a tube with a thicker wall

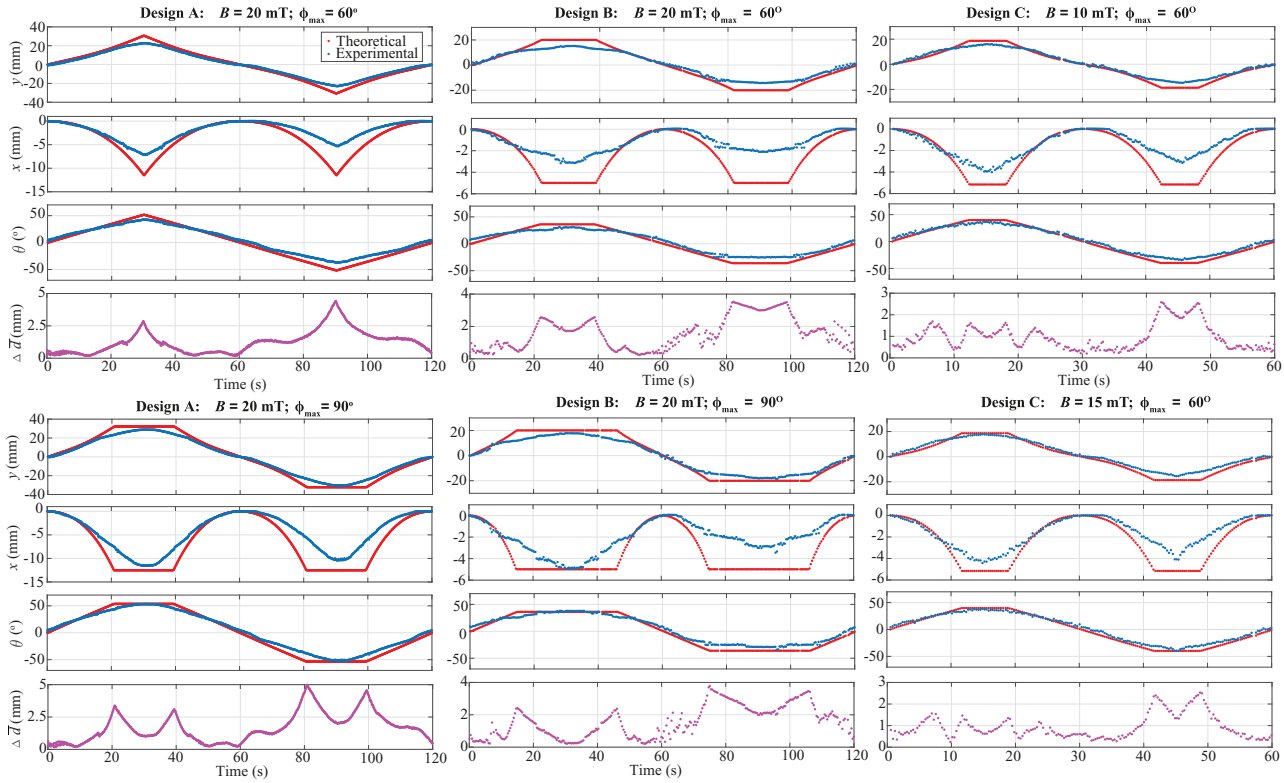

Fig. 7 Plots of *x* coordinate, *y* coordinate, deflection θ, and mean whole shape error $\Delta\bar{d}$ of the three designs of manipulator for the experimental cases of design A: ($B = 20$ mT, $\phi_{max} = 60$ deg, and 90 deg), design B: ($B = 20$ mT, $\phi_{max} = 60$ deg, and 90 deg), and design C: ($B = 10$ mT and 15 mT and $\phi_{max} = 60$ deg)

Table 3 Details of experiments

B (mT)	ϕ_{max} (deg)	θ_{max} (deg)	Δx (mm)	Δy (mm)	$\Delta\theta$ (deg)	$\Delta\,\bar{d}$ (mm)
			Design A			
20	60	42.85	1.2 (1.4)	2.2 (2.3)	5.12 (3.38)	1.1 (0.83)
20	90	53.58	1.8 (1.7)	3.0 (2.5)	5.01 (3.53)	1.5 (1.10)
			Design B			
20	60	31.52	1.4 (1.2)	3.4 (2.2)	6.20 (3.19)	1.5 (0.92)
20	90	38.06	1.4 (1.1)	3.0 (2.2)	5.21 (3.59)	1.3 (0.91)
			Design C			
10	60	37.31	0.77 (0.66)	2.2 (1.6)	4.76 (2.59)	0.98 (0.60)
15	60	39.83	0.72 (0.59)	2.1 (1.5)	4.48 (2.44)	0.94 (0.56)

Note: For strength of magnetic field (B) at maximum angle (ϕ_{max}), maximum angular deflection of manipulator (θ_{max}), and error between theoretical and experimental models for position (Δx and Δy), orientation ($\Delta\theta$) of manipulator tip, and mean whole shape ($\Delta\bar{d}$) are shown in terms of mean values and standard deviation (in brackets).

(increased t), so that the critical buckling load is higher. It is also noticed that the tubes are bent out of the plane of motion, possibly due to stresses during machining. These inaccuracies affect the expected motion of the manipulator.

For magnetic actuation of the manipulator, the use of a permanent magnet and magnetic sheath at its tip is tested (Fig. 2(*c*)). It is observed that the deflection when using permanent magnet is higher than when using magnetic sheath (Fig. 11). This is because of the low magnetic dipole moment (μ) of the magnetic sheath. Therefore, the magnetic sheath is incapable of producing large bends and is restricted to angles below 30 deg. This can be improved by using a magnetic polymer sheath with a greater magnetic dipole moment—using a magnetic powder with a higher residual magnetic field or a higher ratio of powder to polymer. The polymer sheath protects the flexures from the environment without restricting the motion of the manipulator. For medical applications, the replaceable sheath can potentially reduce tissue trauma during steering and can also simplify the sterilization process.

The distal force-bearing capacity of the manipulator is also estimated for potential applications in minimally invasive surgery (please refer to Appendix). Three loading conditions of bending, extension, and compression are considered to obtain the following values, respectively, for design A: 151.67 N, 13.8 N, and 2.45 N; design B: 151.67 N, 22.42 N, and 10.54 N; and design C: 206.83 N, 10.35 N, and 1.92 N. It is found that the bending load is highest of the three, as failure occurs only when the cylindrical wall of the manipulator breaks. The buckling load is the leading potential cause of failure and can be improved by increasing the thickness of the tube. Another potential cause of failure caused by cyclic loading on the flexures is fatigue. Titanium grade 2 has a fatigue strength of 300 MPa at 10^7 cycles unnotched [38]. This stress value is well above the maximum stresses calculated using Eq. (5) for our designs, which are within 120 MPa. Note, it is difficult to estimate the lifetime of the flexure. Besides material properties, fatigue failure also depends on the machining process, surface quality, and operating environment. However, the steering of the manipulator is not expected to generate alternating stresses with large amplitude, suggesting that fatigue failure will not be a significant factor in the design process.

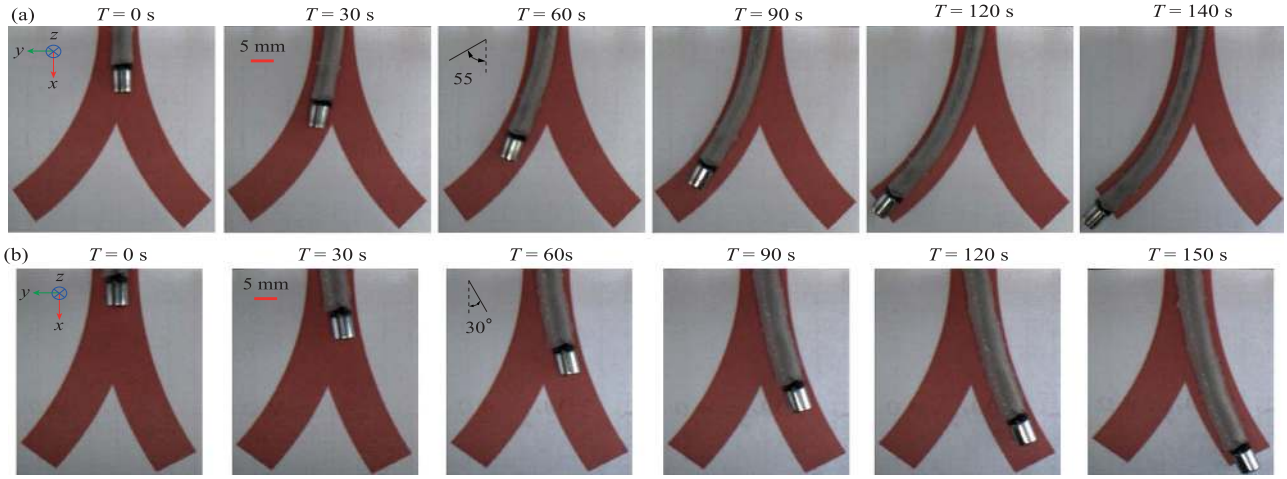

Fig. 8 Illustration of manipulator steering with a polymer sheath around the flexures: six frames for experiment time (*T*) are shown for (*a*) design A following a curvature angle of 55 deg and (*b*) design B following a curvature angle of 30 deg

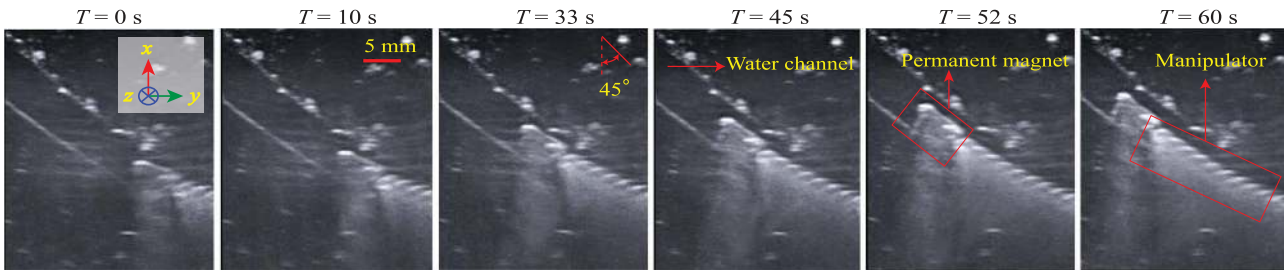

Fig. 9 Ultrasound images acquired during insertion of manipulator through a channel of water in a gelatin phantom

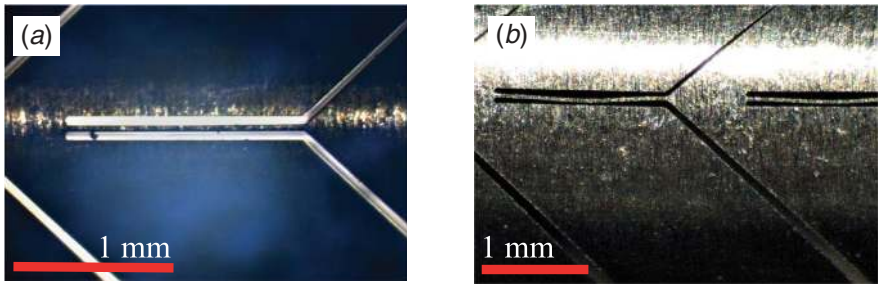

Fig. 10 Microscopic images of metallic tubes showing (*a*) accurately machined flexures and (*b*) inaccurately machined deformed flexures

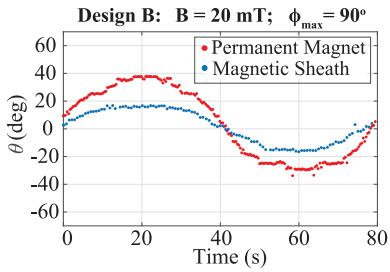

Fig. 11 Plot showing deflection (θ) of design B with a permanent magnet and a magnetic sheath for the experimental case of B = 20 mT, ϕ_{max} = 90 deg

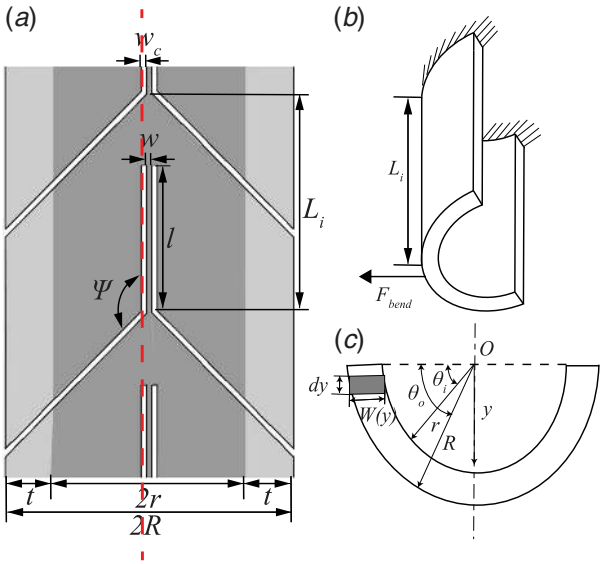

Fig. 12 (*a*) Section view of one segment of the manipulator with a cut made perpendicular to its plane along the dashed line, (*b*) one half of the cut section of the segment, and (*c*) semi-cylindrical cross section of the cut segment

5 Conclusions and Future Work

In this paper, the design of a monolithic metallic compliant continuum manipulator of diameter 3 mm is presented. The performance of the manipulator is evaluated by actuating with a magnetic field up to 20 mT using Helmholtz coils. The three designs, design A with highest width of cut (55 μm), design B with highest width of beam (65 μm), and design C with lowest length of beam (1.1 mm) are tested. The maximum deflection observed is 54 deg for design A, while design B and design C achieved 36 deg and 40 deg bends, respectively. The mean error over three designs in modeling the in-plane position and orientation of the manipulator tip are (1.2 mm and 2.6 mm) and 5.1 deg, respectively, and for whole shape of the manipulator is 1.2 mm. The manipulator steering experiment proves accurate guidance of a manipulator along a path of known curvature using open-loop actuation. The real-time ultrasound visualization of the manipulator inside a gelatin phantom through a water medium shows its clinical feasibility as a steerable surgical manipulator. Contactless actuation of the manipulator is demonstrated by using magnetic field, eliminating the need for a force transmission mechanism. The monolithic design with a small permanent magnet enables easy miniaturization for application as a steerable manipulator in minimally invasive surgical procedures.

In the future work, we plan to improve the fabrication process of the manipulator and improve the accuracy of machining. A two-axis bending design of manipulator will be fabricated to validate the concept of spatial bending. The upgraded design will be tested for higher deflection (>90 deg). Potential applications in endoscopy, biopsy, and ablation will be explored by enhancing the functionality of manipulator. This will be done by embedding additional surgical tools (such as scalpel, retractor, curette, forceps, or scissors) and related sensors (like camera, laser cautery fiber, light, or optical fibers) within its hollow interior. The manipulator steering process will be improved by enabling rotation of the manipulator during insertion. This will be demonstrated in clinically relevant scenarios such as animal tissue or human cadaver studies.

Acknowledgment

G. K. Ananthasuresh thanks Sham Rao of Indian Space Research Organization, with whom the concept of the flexure with restricted bending with a narrow cut was initially developed.

This research has received funding from the European Research Council (ERC) under the European Union's Horizon 2020 Research and Innovation programme (ERC Starting Grant Agreement #638428—project ROBOTAR and ERC Proof-of-Concept Grant Agreement #790088—project INSPIRE).

Appendix: Load Capacity

The distal force-bearing capacity of the manipulator is calculated in this section by considering three different loading conditions during bending, extension, and compression.

Bending Load Capacity. In this case, the manipulator is subjected to bending. If we consider the section view of one segment of the manipulator as shown in Fig. 12, one half of the rigid tube is approximated to have a semi-cylindrical cross section. When the manipulator is bent to its maximum, each section is subjected to a force (F_{bend}) at its end due to contact with the next segment. The bending load capacity will be the maximum value of F_{bend} before failure. For the semi-cylindrical cross section, the centroid

($\bar{y}$) and second moment of area (I) are given by

$$\bar{y} = \frac{\int_0^R y dA}{\int_0^R dA} \tag{A1}$$

$$I = \int_0^R y^2 dA \tag{A2}$$

where $dA = W(y)dy = (R\cos\theta_o - r\cos\theta_i)dy$, $\sin\theta_o = y/R$, $\sin\theta_i = y/r$, $R = 1.5$ mm, and $r = 1$ mm. Substituting these values into Eqs. (A1) and (A2) gives

$$\bar{y} = \frac{\left(\int_0^R yR\sqrt{1-\frac{y^2}{R^2}} - \int_0^r yr\sqrt{1-\frac{y^2}{r^2}}\right)dy}{\left(\int_0^R R\sqrt{1-\frac{y^2}{R^2}} - \int_0^r r\sqrt{1-\frac{y^2}{r^2}}\right)dy} = \frac{4(R^2+Rr+r^2)}{3\pi(R+r)} \tag{A3}$$

$$I = \int_0^R y^2 R\sqrt{1-\frac{y^2}{R^2}}dy - \int_0^r y^2 r\sqrt{1-\frac{y^2}{r^2}}dy = \frac{\pi(R^4-r^4)}{16} \tag{A4}$$

The bending load capacity is given by,

$$F_{bend} = \frac{\sigma_y I}{L_i \bar{y}} \tag{A5}$$

where $\sigma_y = 345$ MPa is the yield strength of titanium. Substituting other parameters, we get the bending loads for the three designs as follows: $F^A_{bend} = 151.67$ N, $F^B_{bend} = 151.67$ N, and $F^C_{bend} = 206.83$ N.

Extension Load Capacity. In this case, the manipulator is subjected to an extension load, which is carried by the flexures. Therefore, the extension load capacity is given by

$$F_{ext} = \sigma_y A \tag{A6}$$

where $A = 2wt = 2w(R-r)$ is the cross-sectional area of the two flexures in a segment. Substituting other parameters, we get the extension load capacity for the three designs as follows: $F^A_{ext} = 13.80$ N, $F^B_{ext} = 22.42$ N, and $F^C_{ext} = 10.35$ N.

Compression Load Capacity. In this case, the manipulator is under compression, and the critical load to be calculated is the buckling load, which is given by the Euler's formula as follows:

$$F_{comp} = P_c r = \frac{\pi^2 EI}{l^2} = \frac{\pi^2 Ew^3 t}{12l^2} \tag{A7}$$

Substituting other parameters, we get the compression load capacity for the three designs as follows: $F^A_{comp} = 2.45$ N, $F^B_{comp} = 10.54$ N, and $F^C_{comp} = 1.92$ N.

References

[1] Chirikjian, G. S., and Burdick, J. W., 1994, "A Hyper-Redundant Manipulator," IEEE Rob. Autom. Mag., **1**(4), pp. 22–29.

[2] Vitiello, V., Lee, S.-L., Cundy, T. P., and Yang, G.-Z., 2012, "Emerging Robotic Platforms for Minimally Invasive Surgery," IEEE Rev. Biomed. Eng., **6**, pp. 111–126.

[3] Bergeles, C., and Yang, G.-Z., 2013, "From Passive Tool Holders to Microsurgeons: Safer, Smaller, Smarter Surgical Robots," IEEE Trans. Biomed. Eng., **61**(5), pp. 1565–1576.

[4] Burgner-Kahrs, J., Rucker, D. C., and Choset, H., 2015, "Continuum Robots for Medical Applications: A Survey," IEEE Trans. Rob., **31**(6), pp. 1261–1280.

[5] Webster, R. J., III, and Jones, B. A., 2010, "Design and Kinematic Modeling of Constant Curvature Continuum Robots: A Review," Int. J. Rob. Res., **29**(13), pp. 1661–1683.

[6] Burgner, J., Swaney, P. J., Lathrop, R. A., Weaver, K. D., and Webster, R. J., 2013, "Debulking From Within: A Robotic Steerable Cannula for Intracerebral Hemorrhage Evacuation," IEEE Trans. Biomed. Eng., **60**(9), pp. 2567–2575.

[7] Gilbert, H. B., Rucker, D. C., and Webster, R. J., III, 2016, "Concentric Tube Robots: The State of the Art and Future Directions" *Robotics Research: The 16th International Symposium ISRR*, Springer, New York, pp. 253–269.

[8] Goldman, R. E., Bajo, A., MacLachlan, L. S., Pickens, R., Herrell, S. D., and Simaan, N., 2012, "Design and Performance Evaluation of a Minimally Invasive Telerobotic Platform for Transurethral Surveillance and Intervention," IEEE Trans. Biomed. Eng., **60**(4), pp. 918–925.

[9] Berthet-Rayne, P., Gras, G., Leibrandt, K., Wisanuvej, P., Schmitz, A., Seneci, C. A., and Yang, G.-Z., 2018, "The I 2 Snake Robotic Platform for Endoscopic Surgery," Ann. Biomed. Eng., **46**(10), pp. 1663–1675.

[10] Saliba, W., Cummings, J. E., Oh, S., Zhang, Y., Mazgalev, T. N., Schweikert, R. A., Burkhardt, J. D., and Natale, A., 2006, "Novel Robotic Catheter Remote Control System: Feasibility and Safety of Transseptal Puncture and Endocardial Catheter Navigation," J. Cardiovasc. Electrophysiol., **17**(10), pp. 1102–1105.

[11] Thomas, D., Scholz, E. P., Schweizer, P. A., Katus, H. A., and Becker, R., 2012, "Initial Experience With Robotic Navigation for Catheter Ablation of Paroxysmal and Persistent Atrial Fibrillation," J. Electrocardiol., **45**(2), pp. 95–101.

[12] Pantos, I., Patatoukas, G., Katritsis, D. G., and Efstathopoulos, E., 2009, "Patient Radiation Doses in Interventional Cardiology Procedures," Curr. Cardiol. Rev., **5**(1), pp. 1–11.

[13] Kim, A. M., Turakhia, M., Lu, J., Badhwar, N., Lee, B. K., Lee, R. J., Marcus, G. M., Tseng, Z. H., Scheinman, M., and Olgin, J. E., 2008, "Impact of Remote Magnetic Catheter Navigation on Ablation Fluoroscopy and Procedure Time," Pacing Clin. Electrophysiol., **31**(11), pp. 1399–1404.

[14] Kota, S., Lu, K.-J., Kreiner, Z., Trease, B., Arenas, J., and Geiger, J., 2005, "Design and Application of Compliant Mechanisms for Surgical Tools," ASME. J Biomech Eng., **127**(6), pp. 981–989.

[15] Howell, L. L., Magleby, S. P., and Olsen, B. M., 2013, *Handbook of Compliant Mechanisms*, John Wiley & Sons, Hoboken, NJ.

[16] Gallego, J. A., and Herder, J., 2009, "Synthesis Methods in Compliant Mechanisms: An Overview," ASME 2009 International Design Engineering Technical Conferences and Computers and Information in Engineering Conference, San Diego, CA, Aug. 30–Sept. 2, pp. 193–214.

[17] Lobontiu, N., 2002, *Compliant Mechanisms: Design of Flexure Hinges*, CRC Press, Boca Raton, FL.

[18] Yin, L., and Ananthasuresh, G., 2003, "Design of Distributed Compliant Mechanisms," Mech. Based Des. Struct. Mach., **31**(2), pp. 151–179.

[19] Swaney, P. J., Burgner, J., Gilbert, H. B., and Webster, R. J., 2012, "A Flexure-Based Steerable Needle: High Curvature With Reduced Tissue Damage," IEEE Trans. Biomed. Eng., **60**(4), pp. 906–909.

[20] Chandrasekaran, K., Sathuluri, A., and Thondiyath, A., 2017, "Magnex—Expendable Robotic Surgical Tooltip," 2017 IEEE International Conference on Robotics and Automation (ICRA), Singapore, May 29–June 3, IEEE, pp. 4221–4226.

[21] Chandrasekaran, K., and Thondiyath, A., 2017, "Design of a Two Degree-of-Freedom Compliant Tool Tip for a Handheld Powered Surgical Tool," ASME J. Med. Devices, **11**(1), p. 014502.

[22] Kim, Y.-J., Cheng, S., Kim, S., and Iagnemma, K., 2012, "Design of a Tubular Snake-Like Manipulator With Stiffening Capability by Layer Jamming," 2012 IEEE/RSJ International Conference on Intelligent Robots and Systems, Vilamoura, Portugal, Oct. 7–12, IEEE, pp. 4251–4256.

[23] Kato, T., Okumura, I., Song, S.-E., Golby, A. J., and Hata, N., 2014, "Tendon-Driven Continuum Robot for Endoscopic Surgery: Preclinical Development and Validation of a Tension Propagation Model," IEEE/ASME Trans. Mechatron., **20**(5), pp. 2252–2263.

[24] Leong, F., Garbin, N., Di Natali, C., Mohammadi, A., Thiruchelvam, D., Oetomo, D., and Valdastri, P., 2016, "Magnetic Surgical Instruments for Robotic Abdominal Surgery," IEEE Rev. Biomed. Eng., **9**, pp. 66–78.

[25] Heunis, C., Sikorski, J., and Misra, S., 2018, "Flexible Instruments for Endovascular Interventions: Improved Magnetic Steering, Actuation, and Image-Guided Surgical Instruments," IEEE Rob. Automat. Mag., **25**(3), pp. 71–82.

[26] Ernst, S., Ouyang, F., Linder, C., Hertting, K., Stahl, F., Chun, J., Hachiya, H., Bänsch, D., Antz, M., and Kuck, K.-H., 2004, "Initial Experience With Remote Catheter Ablation Using a Novel Magnetic Navigation System: Magnetic Remote Catheter Ablation," Circulation, **109**(12), pp. 1472–1475.

[27] Arya, A., Zaker-Shahrak, R., Sommer, P., Bollmann, A., Wetzel, U., Gaspar, T., Richter, S., Husser, D., Piorkowski, C., and Hindricks, G., 2011, "Catheter Ablation of Atrial Fibrillation Using Remote Magnetic Catheter Navigation: A Case–Control Study," Europace, **13**(1), pp. 45–50.

[28] Davis, D. R., Tang, A. S., Gollob, M. H., Lemery, R., Green, M. S., and Birnie, D. H., 2008, "Remote Magnetic Navigation-Assisted Catheter Ablation Enhances Catheter Stability and Ablation Success With Lower Catheter Temperatures," Pacing Clin. Electrophysiol., **31**(7), pp. 893–898.

[29] Edelmann, J., Petruska, A. J., and Nelson, B. J., 2017, "Magnetic Control of Continuum Devices," Int. J. Rob. Res., **36**(1), pp. 68–85.

[30] Boskma, K. J., Scheggi, S., and Misra, S., 2016, "Closed-Loop Control of a Magnetically-Actuated Catheter Using Two-Dimensional Ultrasound Images," 2016 6th IEEE International Conference on Biomedical Robotics and Biomechatronics (BioRob), Singapore, June 26–29, IEEE, pp. 61–66.

[31] Le, V. N., Nguyen, N. H., Alameh, K., Weerasooriya, R., and Pratten, P., 2016, "Accurate Modeling and Positioning of a Magnetically Controlled Catheter Tip," Med. Phys., **43**(2), pp. 650–663.

[32] Venkiteswaran, V. K., Sikorski, J., and Misra, S., 2019, "Shape and Contact Force Estimation of Continuum Manipulators Using Pseudo Rigid Body Models," Mech. Mach. Theory, **139**, pp. 34–45.
[33] Chautems, C., Tonazzini, A., Floreano, D., and Nelson, B. J., 2017, "A Variable Stiffness Catheter Controlled With An External Magnetic Field," 2017 IEEE/RSJ International Conference on Intelligent Robots and Systems (IROS), Vancouver, BC, Canada, Sept. 24–28, IEEE, pp. 181–186.
[34] Liu, T., Lombard Poirot, N., Greigarn, T., and Cenk Çavuşoğlu, M., 2017, "Design of a Magnetic Resonance Imaging Guided Magnetically Actuated Steerable Catheter," ASME J. Med. Devices, **11**(2), p. 021004.
[35] Sikorski, J., Rutting, E. S., and Misra, S., 2018, "Grasping Using Magnetically-Actuated Tentacle Catheter: A Proof-of-Concept Study," 2018 7th IEEE International Conference on Biomedical Robotics and Biomechatronics (Biorob), Enschede, Netherlands, Aug. 26–29, IEEE, pp. 609–614.
[36] Howell, L., 2001, *Compliant Mechanisms*, Wiley, New York.
[37] Venkiteswaran, V. K., Samaniego, L. F. P., Sikorski, J., and Misra, S., 2019, "Bio-Inspired Terrestrial Motion of Magnetic Soft Millirobots," IEEE Rob. Automat. Lett., **4**(2), pp. 1753–1759.
[38] ASM Aerospace Specification Metals Inc., "Titanium grade-2," http://asm.matweb.com/search/SpecificMaterial.asp?bassnum=MTU020, Accessed March 19, 2020.